J. Fluid Mech. (1998), *vol.* 372, *pp.* 165–187. Printed in the United Kingdom

Formation of a jump by the dam-break wave over a granular bed

By H. CAPART[1] AND D. L. YOUNG[2]

[1]Department of Civil Engineering, Université Catholique de Louvain, and Fonds National de la Recherche Scientifique, Belgium

[2]Department of Civil Engineering and Hydraulic Research Laboratory, National Taiwan University, Taipei, Taiwan

(Received 3 January 1997 and in revised form 17 April 1998)

A previously unreported shock feature associated with the scouring of a horizontal granular bed by a dam-break wave is discussed. Near the wave centre, the present study shows, the free surface breaks backward and a hydraulic jump forms. This behaviour is described from the standpoint of shallow-water theory, suitably extended to deal with non-equilibrium sediment transport. The shock formation involves a particularly strong coupling between flow free-surface evolution and bed morphodynamics. Support for our conclusions is sought through experimental and numerical approaches. In order to magnify the observed phenomena, measurements were performed for the case of light bed particles moving in sheet and debris flow modes. A detailed picture of the transient two-phase flow is presented, based on whole field acquisition of the grain motions by particle tracking techniques. Corresponding shallow-water solutions are constructed numerically using a shock capturing scheme. Finally, an interpretation of the jump formation is proposed based on the theory of characteristics.

1. Introduction

The sudden collapse of a dam results in a highly unsteady flow. In this paper, we examine what occurs when such a severe transient develops over a loose granular bed. The problem considered is two-dimensional in the vertical plane, with an initially horizontal stream bottom. An idealized dam separates an upstream body of quiescent water from a downstream region of zero water depth. The water table downstream does however come up to the channel level, thereby saturating the porous bottom (figure 1). The bed extending on both sides of the dam is composed of cohesionless granular material. After the rapid removal of the dam, an intense two-phase flow can be observed.

Over a rigid horizontal bed that is originally dry below the dam, the two-dimensional dam-break flow is well known to exhibit a continuous, monotonic decrease in free surface from upstream to downstream (Stoker 1948, 1957; Dressler 1952, 1954). In the present work, the significantly different behaviour which arises over a mobile bed is documented. Sediment particles are swiftly eroded and convected away by the dam-break wave. In turn, the bed evolution induces changes in the gravity-driven flow. This interaction leads to the formation of a hydraulic jump near the centre of the dam-break wave. Generation of this secondary shock constitutes a distinctive feature of the dam-break wave over granular bed.

The problem is of much practical significance, since a dam-break wave in a natural valley will erode the river bed and convey downstream the materials of the dam itself (Takahashi & Nakagawa 1994). As witnessed in the case of the Macchu II dam failure in India (Havnø 1995), interactions with the bed can also seriously compound flood damage. The overtopping of a dyke (Visser, Vrijling & Verhagen 1990) or the breach of a caldera lake (Waythomas *et al.* 1996) are other instances of catastrophic flooding where sediment transport plays an important role. In some cases, redistribution of bed sediment material is the objective pursued in triggering fast water transients. This was recently illustrated by the large-scale artificial flash floods induced in the Colorado River downstream of Glen Canyon Dam (US Department of the Interior 1996). A sewer flush flow released to cleanse solid deposits is an example of a smaller scale, more common application (Capart, Sillen & Zech 1997).

Beyond its importance as a practical problem, the dam-break wave over a granular bed is interesting as a case study of key processes associated with shallow-water sediment transport. Non-equilibrium transport is said to occur whenever the solid load is unable to adapt instantaneously to sharp spatial or temporal variations in the flow. On the other hand, the possible breaking of the free surface into hydraulic jumps or bores constitutes a fundamental trait of shallow-water waves. Clearly, shock singularities create a situation in which sediment transport will deviate from equilibrium conditions. In return, deformation of the bed is one of the mechanisms which can lead to the formation of shocks. Thus, the jump which characterizes the dam-break wave over a granular bed can be related to more general physical processes. Interaction between non-equilibrium sediment transport and hydrodynamic shocks is also exhibited, for instance, by the bores of the coastal surf zone, or the periodic wave breaking which curtails the growth of antidunes.

In order to enhance the effects of the interplay, we investigate the interactions of the dam-break wave with a light, highly mobile bed material. This results in high-intensity sediment transport, moving as sheet flow and debris flow. These modes of transport occur in conjunction with fast flows, and are most likely to be encountered in situations such as flash floods, mountain landslides and surf zone waves. They have been the subject of much recent research (see e.g. Dick & Sleath 1991; Takahashi 1991; Asano 1995; Sumer *et al.* 1996). New possibilities for the experimental characterization of these modes of transport are offered by imaging methods. The present research uses tracking techniques to obtain a whole-field characterization of the grain motions, from which estimates of the instantaneous sediment transport across arbitrary cross-sections can be derived.

In this study, we seek to understand the above mentioned processes in reference to shallow-water theory, extended to encompass non-equilibrium, high-intensity sediment transport. This involves coupling the Saint-Venant equations with a bed-level evolution equation, as well as with an advection-reaction equation accounting for the sediment transport and the non-equilibrium mass exchange between sediment bed and sediment-laden flow. Both mathematical implications and physical interpretations of the theory are analysed in relation to the dam-break wave over granular bed problem.

The paper is organized as follows. Section 2 covers the theoretical framework, including governing equations, constitutive relations and numerical method of solution. Section 3 details the experimental apparatus, analysis techniques and observed results. The laboratory measurements are compared in §4 with numerical solutions. Finally, the flow features are interpreted in §5 from the standpoint of the theory of characteristics.

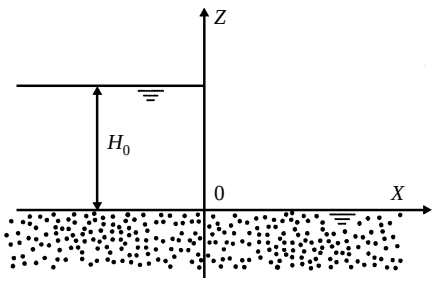

FIGURE 1. Idealized dam-break wave over a granular bed: sketch of the initial conditions.

2. Mathematical formulation

2.1. *Governing equations*

We consider the following shallow-water, non-equilibrium transport formulation. In conservation form and dimensional variables, vertically averaged evolution equations are written

$$\frac{\partial H}{\partial T} + \frac{\partial (HV)}{\partial X} = -\frac{\partial Z_b}{\partial T}, \tag{2.1a}$$

$$\frac{\partial (\rho HV)}{\partial T} + \frac{\partial (\rho HV^2 + \frac{1}{2}\rho g H^2)}{\partial X} = -\rho g H \frac{\partial Z_b}{\partial X} - \tau_b, \tag{2.1b}$$

$$\frac{\partial H_B}{\partial T} + \frac{\partial (H_B V_B)}{\partial X} = \frac{1}{T_{bB}}(H_B^{\mathrm{eq}} - H_B) = N_{bB}, \tag{2.1c}$$

$$\frac{\partial Z_b}{\partial T} = -\frac{1}{c_b} N_{bB}. \tag{2.1d}$$

In the above equations, T = time; X = distance; H = flow depth; V = vertically averaged horizontal velocity; suffices b and B respectively refer to the motionless bed and the moving bed material; Z_b = bed elevation; τ_b = bed shear stress; $\rho = \rho_w\big(1+(s-1)H_B/H\big)$ = density of the water–sediment mixture, with ρ_w = density of water, ρ_s = sediment density, and $s = \rho_s/\rho_w$ = specific gravity of sediment grains; H_B = sediment load, i.e. volume of moving bed material per unit bed surface; H_B^{eq} = sediment load under steady uniform equilibrium conditions; V_B = mean velocity of the moving sediment load; N_{bB} = rate of sediment exchange between bed and flow, i.e. net volume of bed material transferred to the flow per unit time and unit bed surface; g = acceleration due to gravity; T_{bB} = relaxation time associated with sediment exchange between bed and flow; c_b = volume concentration of sediment in the undisturbed bed.

Corresponding initial conditions for the dam-break case (see figure 1) are given by

$$H(X,0^-) = \begin{cases} H_0, & X \leqslant 0 \\ 0, & X > 0, \end{cases} \tag{2.2a}$$

$$V(X,0^-) = 0, \qquad X \leqslant 0, \tag{2.2b}$$

$$H_B(X,0^-) = 0, \quad Z_b(X,0^-) = 0, \tag{2.2c,d}$$

where H_0 is the initial depth of quiescent water upstream of the dam. As the initial conditions extend infinitely, we have a pure initial value problem which does not require specification of boundary conditions.

A system of equations similar to (2.1) has been given by Phillips & Sutherland (1989) in one-dimensional, non-conservative form, and by Takahashi & Nakagawa (1994) in depth-averaged, horizontal two-dimensional form. Equations (2.1*a*) and (2.1*b*) are the vertically averaged shallow-water (Saint-Venant) equations written for the water–sediment mixture. The additional source term $\partial Z_b/\partial T$ in (2.1*a*) accounts for volume transfer between bed and flow. In contrast with Takahashi & Nakagawa (1994), the non-homogeneous density of the water–sediment mixture has been taken into account in (2.1*b*). Due to the high-intensity solid transport and the strong sediment concentration gradients, the influence of density variations on the momentum balance of the flow is significant in the present case. Vertical accelerations as well as velocity variations over a vertical have been neglected and the usual (long wave) shallow-water hypothesis is considered valid (see Stoker 1957; Whitham 1974).

Volume conservation of bed material is divided into two components. The advection-reaction equation (2.1*c*) governs the evolution of the volume of particles moving with the flow, while equation (2.1*d*) describes the evolution of the volume of non-moving bed particles. Combining (2.1*c*) and (2.1*d*) results in the Exner equation expressing global conservation of sediment. The rate of sediment exchange between bed and flow N_{bB} is assumed proportional to the difference between the actual instantaneous sediment load and the equilibrium sediment load under corresponding uniform flow conditions. This constitutes a non-equilibrium relationship (Einstein 1920) of a form widely used in non-equilibrium thermodynamics (see Reif 1965) and multiphase flow (Bauer, Houdayer & Sureau 1976), where it can be derived using boundary layer or statistical arguments. Based upon the stochastic bedload description of Einstein (1950), Tsubaki & Saito (1967) appear to be the first investigators to have applied the concept to sediment transport (see also Phillips & Sutherland 1989).

The evolution equations constitute a hyperbolic system of conservation laws of a kind widely encountered in mathematical physics (see Kevorkian 1990). The theory of characteristics constitutes a powerful tool for their interpretation and solution (for a classical presentation, see Stoker 1957; a recent account is given by Liggett 1994). Due to their hyperbolic nature, the partial differential equations can be transformed into a set of ordinary differential equations, or compatibility equations, to be integrated along characteristic paths. In our case, these characteristic paths are defined by

$$\Lambda_+ : \frac{\mathrm{d}X}{\mathrm{d}T} = V + (gH)^{1/2}, \tag{2.3a}$$

$$\Lambda_- : \frac{\mathrm{d}X}{\mathrm{d}T} = V - (gH)^{1/2}, \tag{2.3b}$$

$$\Lambda_B : \frac{\mathrm{d}X}{\mathrm{d}T} = V_B, \tag{2.3c}$$

$$\Lambda_b : \frac{\mathrm{d}X}{\mathrm{d}T} = 0. \tag{2.3d}$$

In writing (2.3*a*) and (2.3*b*), we have neglected the effects of non-homogeneous density, so that the corresponding characteristics are identical to the rigid bed case.

The characteristics lend themselves well to physical interpretation. The first two families of characteristics Λ_+ and Λ_- represent the propagation of small hydrodynamic disturbances ahead of the current and against it respectively. Characteristics of the Λ_B family associated with the advective sediment transport are simply the pathlines of moving grains. Finally, family Λ_b corresponds to bed elevation change.

The vertical trajectories of Λ_b in the (X, T)-plane reflect the slow propagation of bed disturbances in comparison with their hydrodynamic counterparts.

A physically significant property of hyperbolic systems lies in the possible development of discontinuous solutions. These mathematical discontinuities, or shocks, form where characteristic paths of the same family intersect (see e.g. Abbott 1979). In such an event, partial differential equations (2.1) no longer apply, and instead shock (Rankine–Hugoniot) relations must be enforced. Excluding discontinuities in the bed profile, the relations are written

$$a = \frac{\Delta(HV)}{\Delta H}, \quad a = \frac{\Delta(\rho HV^2 + \frac{1}{2}\rho g H^2)}{\Delta(\rho HV)}, \quad a = \frac{\Delta(H_B V_B)}{\Delta H_B}, \tag{2.4a,b,c}$$

where a is the propagation velocity of the discontinuity. The general problem of describing the evolution of the flow–bed system is thus one of constructing weak solutions to system (2.1), i.e. solutions complying with (2.1) over smooth regions, and respecting shock conditions (2.4) across discontinuities.

The evolution equations (2.1) can be non-dimensionalized as follows. Initial depth H_0 is chosen as a characteristic dimension for the flow. Dimensionless variables can be defined according to Froude similarity as

$$t = \left(\frac{g}{H_0}\right)^{1/2} T, \quad x = \frac{X}{H_0}, \quad h = \frac{H}{H_0}, \quad v = \frac{V}{(gH_0)^{1/2}}, \tag{2.5a–d}$$

$$h_B = \frac{H_B}{H_0}, \quad v_B = \frac{V_B}{(gH_0)^{1/2}}, \quad z_b = \frac{Z_b}{H_0}, \quad r = \frac{\rho}{\rho_w}. \tag{2.5e–h}$$

System (2.1) can then be cast in the following dimensionless form:

$$\frac{\partial h}{\partial t} + \frac{\partial (hv)}{\partial x} = -\frac{\partial z_b}{\partial t}, \tag{2.6a}$$

$$\frac{\partial (rhv)}{\partial t} + \frac{\partial (rhv^2 + \frac{1}{2}rh^2)}{\partial x} = -rh\frac{\partial z_b}{\partial x} - \mu h_B, \tag{2.6b}$$

$$\frac{\partial h_B}{\partial t} + \frac{\partial (h_B v_B)}{\partial x} = \frac{\kappa}{v}(\varepsilon v^2 - h_B) = n_{bB}, \tag{2.6c}$$

$$\frac{\partial z_b}{\partial t} = -\frac{n_{bB}}{c_b}, \tag{2.6d}$$

where we have introduced the three non-dimensional parameters

$$\mu = \frac{\tau_b}{\rho_w g H_B}, \quad \kappa = \frac{V}{g T_{bB}} \quad \varepsilon = \frac{H_B^{\mathrm{eq}}}{V^2/g}, \tag{2.7a,b,c}$$

which can be interpreted respectively as bed friction, sediment exchange and sediment mobility coefficients. Choice of these parameters will be justified in §2.2 below where we derive scaling laws for the constitutive relations.

2.2. *Scaling of the constitutive relations*

Closure of the governing equations (2.1) requires the additional specification of constitutive relations. These are to relate H_B^{eq}, V_B, τ_b and T_{bB} to bed material characteristics and local hydrodynamic conditions. At the moderate rates of transport commonly encountered in sediment transport studies, a key role in this respect is often assigned to the Shields number

$$\Psi = \frac{\tau_b}{\rho_w g(s-1)D}. \tag{2.8}$$

The Shields number normalizes the bed shear stress with respect to the grain size D and the sediment specific gravity s, and usually serves as argument of a functional relationship which allows prediction of the sediment transport rate. For the high rates of transport associated with sheet and debris flow conditions, however, the bed shear stress τ_b and therefore the Shields number are themselves dependent on the intensity of sediment transport, inducing a cumbersome feedback in the relationships. Hence, following Asano (1995), we prefer to resort to the mobility number

$$\Theta = \frac{\frac{1}{2}V^2}{g(s-1)D} \tag{2.9}$$

expressed directly in terms of vertically-averaged velocity V.

A normalized equilibrium sediment transport rate defined after Einstein (1950) as

$$\Phi^{\mathrm{eq}} = \frac{H_B^{\mathrm{eq}} V_B}{\left(g(s-1)D^3\right)^{1/2}} \tag{2.10}$$

is shown by Asano (1995) to scale well with the mobility number according to

$$\Phi^{\mathrm{eq}} \propto \Theta^{3/2}. \tag{2.11}$$

This is consistent with the report by Ribberink & Al-Salem (1990) that the sediment transport rate under sheet-flow conditions shows a distinct linear relationship with the third power of the main stream velocity amplitude.

Bed shear stress can be split into two components (Bagnold 1954; see also Fredsøe & Deigaard 1992) according to

$$\tau_b = \tau_{bB} + \tau' \tag{2.12}$$

where τ_{bB} is due to collisions between grains, and τ' is the residual stress due to momentum transfer within the interstitial fluid, negligible if particles are closely packed. In the present case of sheet- and debris-flow sediment transport, intergranular contacts provide the dominant mechanism of support for the solid phase. For an essentially horizontal flow, the submerged weight of moving particles above bottom level Z_b must therefore be in equilibrium with an intergranular normal stress σ_{bB} (Bagnold 1956; Nnadi & Wilson 1992), according to

$$\sigma_{bB} = \rho_w g(s-1)H_B. \tag{2.13}$$

The existence of such a normal stress was demonstrated by Bagnold (1954), who proposed describing it as a dispersive pressure due to interparticle collisions within the rapidly sheared medium. In addition, Bagnold showed the grain shear stress to be proportional to the normal stress following

$$\tau_{bB} = \tan\alpha\ \sigma_{bB}, \tag{2.14}$$

where α can be viewed as a dynamic friction angle and $\tan\alpha$ has an experimental value of 0.32 in the high-speed (grain-inertia) range. From (2.12), (2.13) and (2.14), and neglecting τ', we obtain for τ_b the relation

$$\tau_b = \tan\alpha\ \rho_w g(s-1)H_B, \tag{2.15}$$

in which bed resistance is linked to the solid load H_B. Non-dimensional friction factor μ is therefore related to Bagnold's dynamic friction angle according to

$$\mu = \tan\alpha\ (s-1). \tag{2.16}$$

At low rates of transport, the mean velocity of the moving grains V_B should be less than the mean flow velocity. At the very high rates which characterize the tip of a debris flow, however, the two are expected to become equal (this is verified in §3.3 where the experimental results are analysed). Since the influence of the wave tip dominates the overall transport process in the dam-break wave case, in this study we simply consider the identity

$$V_B = V. \tag{2.17}$$

For bedload transport close to threshold conditions and in the case of erosion of the channel bed, the relaxation time T_{bB} has been found by investigators (Fernandez-Luque & van Beek 1976; Phillips & Sutherland 1989) to vary as

$$T_{bB} = \frac{\ell}{V_B}, \tag{2.18}$$

where ℓ is a relaxation length proportional to grain diameter D. Under assumptions valid for low rates of transport with individual grains moving in a succession of irregular discrete steps, ℓ represents the mean length travelled by a particle in a single trajectory before it comes to rest. At the high rates of transport of sheet and debris flow, however, we expect this relaxation length to scale instead with the equilibrium thickness of the sheet layer δ_B^{eq}. This thickness is shown by Wilson (1987) to be related to the Shields number according to

$$\frac{\delta_B^{\mathrm{eq}}}{D} \propto \Psi. \tag{2.19}$$

Since roughness velocity approximately varies linearly with main stream velocity, a similar scaling is obtained in terms of mobility number as

$$\frac{\delta_B^{\mathrm{eq}}}{D} \propto \Theta. \tag{2.20}$$

We therefore obtain for T_{bB} the scaling

$$T_{bB} \propto \frac{\Theta D}{V_B} \propto \frac{V}{g(s-1)}. \tag{2.21}$$

This is identical in form (with the mobility number replacing the Shields number) to the lag relationship given by Phillips & Sutherland (1989) and resulting from Yalin's (1972) estimate of the average step length of grains as $\ell \propto \Psi D$.

In terms of dimensionless coefficients μ, κ and ε, the scalings can be rewritten

$$\mu \propto (s-1), \quad \kappa \propto (s-1), \quad \varepsilon \propto (s-1)^{-1}. \tag{2.22a,b,c}$$

Thus under high-intensity transport, the equations governing the dam-break wave over a granular bed, when scaled according to Froude similarity, are independent of the roughness ratio D/H_0. In other words the relative size of the sediment grains is expected to exert only a minor influence on the behaviour of the two-phase flow. Submerged weight represented by the difference $(s-1)$, by contrast, constitutes a key factor. In particular, specific gravity s controls the mobility of the bed material. Choice of a light sediment is therefore an effective way of magnifying the effects of flow–bed interaction.

2.3. *Numerical method*

Different numerical methods exist which can be used to solve hyperbolic systems of conservation laws. The scheme adopted in the present study is a generalization

(Capart 1996) of an explicit finite difference algorithm originally developed by Braschi & Gallati (1992) for shallow water flow over a rigid bed. It is part of the family of upwind schemes which, building upon the work of Lax (1954), have been devised to automatically capture propagating shocks (for a review, see Harten, Lax & van Leer 1983).

The evolution equations in forms (2.1) or (2.6) can be written in vector form

$$\frac{\partial \boldsymbol{U}}{\partial T} + \frac{\partial \boldsymbol{F}(\boldsymbol{U})}{\partial X} = \boldsymbol{S}(\boldsymbol{U}), \tag{2.23}$$

where $\boldsymbol{U}$, $\boldsymbol{F}$ and $\boldsymbol{S}$ can respectively be interpreted as density, flux and source terms.

The key statement of the numerical algorithm is then

$$U_i^{j+1} = U_i^j + \frac{\Delta T}{\Delta X}\left(F^*_{i-1/2} - F^*_{i+1/2}\right) + \Delta T\, S_i, \tag{2.24}$$

in which indice i denotes one of the cells of the spatial discretization, indices $i-1/2$ and $i+1/2$ refer to the upstream and downstream boundaries of the cell, and indices j and $j+1$ denote values of the variables at times T and $T+\Delta T$. Flux terms F^* are to be predicted from the known values of the density and source terms at time T. In the present mobile bed extension, this is achieved by solving simplified compatibility equations along approximated characteristic paths. Accordingly, a physically sound signal propagation is guaranteed. The scheme can thus accommodate both subcritical and supercritical regimes of flow as well as regime transitions.

The dry bed at the tip of the wave is not considered a moving boundary. Rather, a small fictitious depth ($= H_0/1000$) is imposed in the region downstream from the dam. Simulations end before the negative and positive waves reach the upstream or downstream limits of the computational domain, so that no special treatment of boundary conditions is required.

Stability of the explicit scheme is subject to the Courant–Friedrichs–Lewy (CFL) condition expressed by

$$Cr = \frac{\max_i\left(V_i + (gH_i)^{1/2}\right)}{\Delta X/\Delta T} < 1, \tag{2.25}$$

where Cr is the Courant number. The complete scheme was tested on a number of benchmark tests and found to produce accurate, well-behaved solutions.

3. Experiments

3.1. *Physical set-up and instrumentation*

A 12 m long, 70 cm high, and 20 cm wide flume was employed for the experiments. Light artificial pearls of uniform size were selected as bed particles with the objective of obtaining a moving layer as thick as possible and particle motions that could be reliably tracked on digital images. Particle characteristics are as follows: diameter $D =$ 6.1 mm, specific gravity $s = 1.048$, and fall velocity in water (at 23°C) $\omega = 7.6$ cm s^{-1}.

The mobile bed reach covered by the measurements was 1.20 m long, with a particle layer 6 cm deep. These dimensions were chosen to allow the dam-break wave and scour hole to develop unconstrained over a sufficient length of time. Volumetric sediment concentration of the undisturbed bed was estimated as $c_b = 0.4$. To prevent bottom slippage, a metal mesh with mesh size approximately equal to the diameter of the particles was placed under the mobile layer.

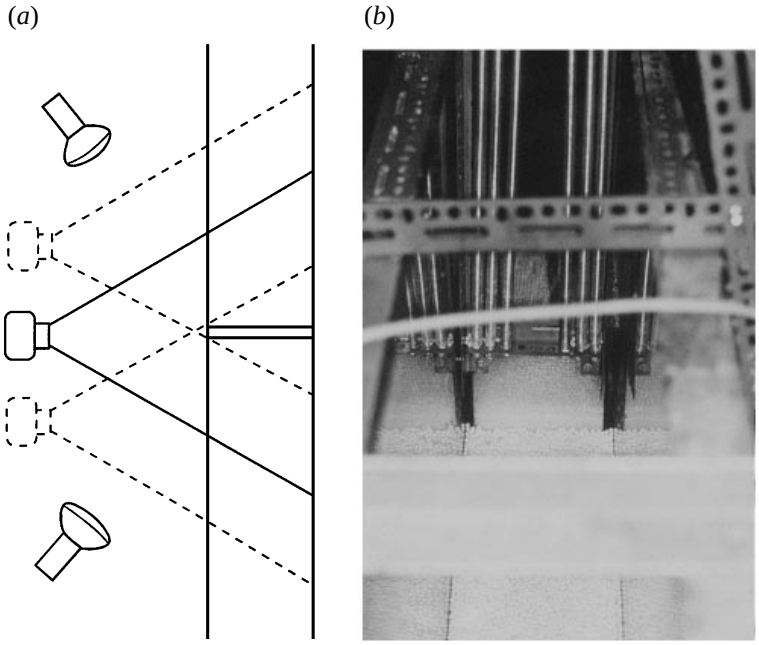

FIGURE 2. Experimental set-up: (*a*) camera and lighting configuration; (*b*) top view of the flume, sluice gate and particle bed.

A Perspex sluice gate with flexible lateral and bottom joints was used as the idealized dam. Special care was taken to adjust the joints in order to prevent small water leaks from causing seepage, hence disrupting the downstream granular bed. For each run, water was introduced downstream from the gate up to the bed level and upstream up to the desired water depth. The granular bed was profiled to define a horizontal surface on both sides. The gate was then rapidly raised (within 50 ms) by a system of springs, and the resulting two-phase flow was observed. A photograph of the physical set-up is shown on figure 2.

The flow was filmed from the side through the flume's transparent walls with lighting provided by two 500 W projectors. The image acquisition system was composed of a charge-coupled device (CCD) camera linked to a PC-controlled frame grabber board. Images were acquired at a rate of 100 frames per second and have a resolution of 256 $\times$ 256 pixels $\times$ 256 levels of grey. To obtain a suitable level of detail, only a limited viewing window could be filmed for each run. Experiments were thus repeated a number of times with different camera positions in order to recompose the evolution of the entire flow field (see figure 2*a*).

3.2. *Digital image analysis*

In the present work, image analysis is used both to trace the free-surface evolution and to track the motion of individual grains. The two measurement types were pioneered early. Dressler (1954) used motion picture photography to capture the free-surface evolution of the dam-break wave over rigid bed. Fernandez-Luque & van Beek (1976) and Nakagawa, Tsujimoto & Miyamoto (1978) analysed film sequences in order to characterize bedload sediment transport. New methods have arisen in the wake of recent progress in digital sensor technology and image processing techniques. A general review of particle-imaging methods is given by Adrian (1991), while recent

examples of sediment transport studies involving digital imaging techniques are found in Nakagawa, Tsujimoto & Gotoh (1992), Lee & Hsu (1994) and Adriaens & van Rillaer (1996).

High-intensity sediment transport poses two specific challenges to digital imaging techniques. First, analysis is hindered by a non-uniform dispersion of particles presenting regions of very dense packing. Secondly, the concentrations as well as the velocities of the moving sediment grains are to be extracted from the images. Special techniques were therefore used. The analysis procedure involves the following steps: (i) identification of the particles; (ii) tracking, or matching of particles between successive frames; (iii) construction of velocity and concentration field representations; and (iv) extraction of aggregate measurements from the field representations. As they are detailed elsewhere (Capart *et al.* 1997), these steps are only briefly introduced here.

Identification of the particles (with diameters corresponding to approximately 5 pixels on the digital images) was carried out by taking advantage of their spherical shape. A local mask was applied to highlight the regions of maximum radial symmetry with peaks corresponding to particle centroids. The method was found to reliably and exclusively identify particles even when the illumination was not entirely uniform within the imaging window. While more elaborate algorithms exist (see e.g. Jähne 1991; Jain, Kasturi & Schunck 1995), the matching of particles from one image to the next was performed in this study using a first-order predictor-corrector procedure. This relatively simple method required manual supervision in regions of steeper velocity gradients.

Sediment concentration was estimated from the particle positions identified on the images. Transformation from a discrete set of positions to a continuous concentration field was achieved by applying the following procedure. A triangular mesh is first constructed and optimized with nodes located at particle centres. A surface density η is then obtained by assigning one half-particle to the surface of each triangle. If the mesh is considered to be a set of constant elements, this method presents the desirable property of preserving exact conservation, i.e. integrating the density over the whole surface yields the original number of particles identified on the image. This surface concentration (= a number of particles per unit surface) is transformed into volumetric concentration c by applying a relation inspired by Bagnold (1954):

$$\frac{c}{c_0} = \left(\frac{\eta}{\eta_0}\right)^{3/2}, \tag{3.1}$$

where $c_0 = \pi/3\sqrt{2} \approx 0.74$ and $\eta_0 = \sqrt{2}/D^2$ correspond, via elementary geometrical considerations, to the tetrahedral-rectangular piling of perfect spheres of uniform diameter D (i.e. the arrangement which yields the maximum packing). Relationship (3.1) is strictly valid only in the limit of high grain concentration when the distance between particles becomes close to their diameter. It is a reasonable approximation for the present experiments because the dominant transport occurs in very dense modes.

Likewise, measured velocity vectors are assigned to the mesh nodes. Aggregate measurements are then easily derived from the velocity and concentration fields. In particular, the instantaneous sediment transport rate (per unit width) at any cross-section is obtained by vertically integrating the product of grain concentration and horizontal velocity. Results obtained using the above methods were subjected to various validation tests detailed in Capart & Young (1997). Despite the inherently random behaviour of the particles, the measurements for the sediment fluxes were found to be reproducible and consistent with conservation constraints.

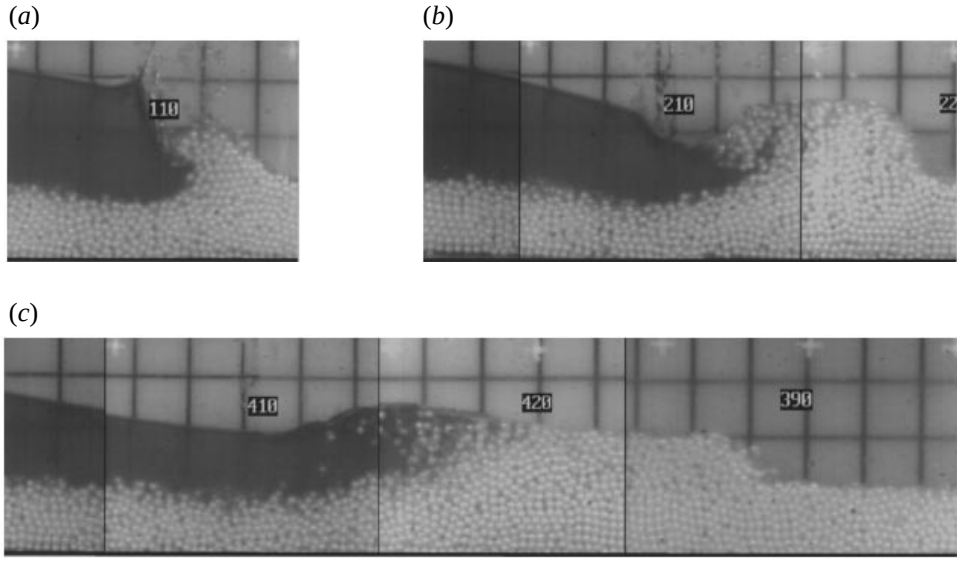

FIGURE 3. Selected digital frames for wave of initial depth $H_0 = 10$ cm: (*a*) dimensionless time $t = 1$; (*b*) $t = 2$; (*c*) $t = 4$. For spatial references, see figure 4.

3.3. *Results and discussion*

Figure 3 presents composites of digital images obtained for the dam-break wave of initial depth $H_0 = 10$ cm at non-dimensional times $t = 1$, 2 and 4. The white particles contrast well against the dark surrounding water in the images, and the free surface is easily discerned from the back-illumination grid. Corresponding particle velocity fields and free surface profiles are given in figure 4. For reference, the initial gate position, bed profile and water surface are shown in dashed lines.

Convective transport of the bed material is clearly depicted. As the dam-break wave develops, bed particles are lifted by the flow and carried downstream. The most severe grain entrainment occurs in the vicinity of the original dam (located at $X = 0$) where the formation of a scour hole results. Material eroded in this way is transported with highest intensity near the fast moving wave front, with densely packed grains occupying the whole flow depth. The mechanism of sediment transport thus evolves from sheet flow upstream to fully developed debris flow towards the wave tip.

The forefront of the dam-break wave behaves as a typical debris flow (Hirano & Iwamoto 1981; Suwa 1988; see also Takahashi 1991). Under the combined effects of bed resistance and incorporation of bed material into the flow, the free surface steepens at the wave tip. Intense grain–grain interactions, which provide the mechanism of support for the moving sediment, are also highly effective in redistributing horizontal momentum over depth. This translates into particle velocity profiles that become increasingly uniform towards the front of the wave. The net result is a nearly vertical wall of water and debris which overruns the granular bed.

The most striking feature of the flow shown on figures 4 and 5 is the formation of a hydraulic jump near the wave centre (at the initial location of the dam). A rapidly varied free surface, along with near-surface turbulence and irregular waves radiating energy downstream (Benjamin & Lighthill 1954), are conspicuous jump characteristics. They can be linked (see Longuet-Higgins 1992; Lin & Rockwell 1995) to an injection of vorticity into the flow as a result of the strong curvature of the

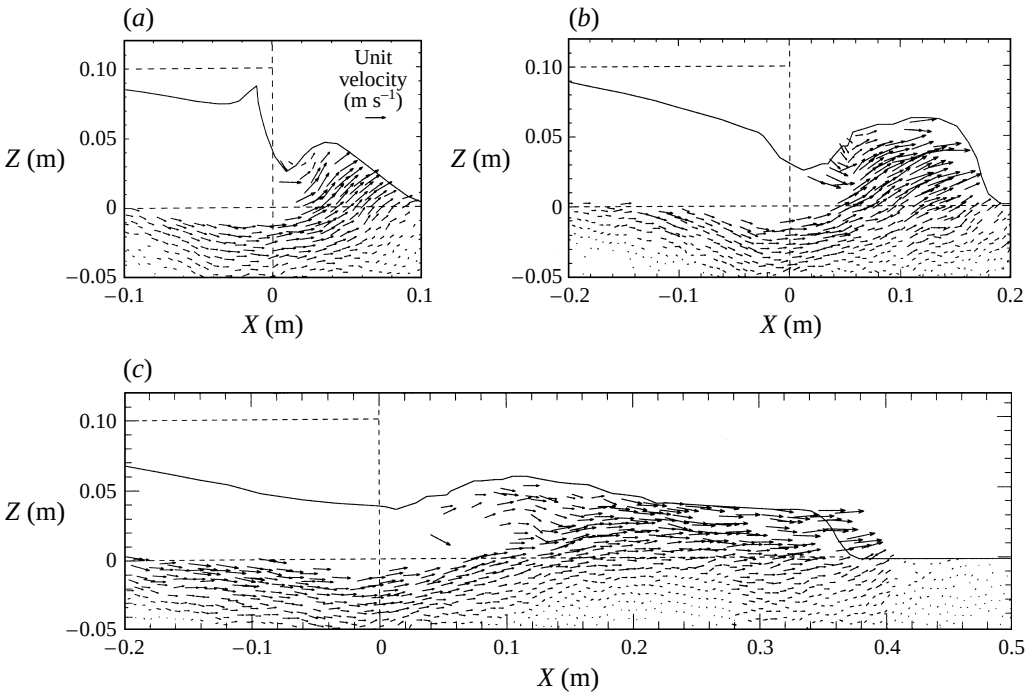

FIGURE 4. Evolution of the free-surface profile and particle velocity field for wave of initial depth $H_0 = 10$ cm: (*a*) dimensionless time $t = 1$; (*b*) $t = 2$; (*c*) $t = 4$; - - - - -, initial gate position, bed profile and water surface.

air–water interface. A group of particles is observed to be temporarily held captive within the jump recirculation zone. The gradual growth and enduring character of the jump feature make it highly unlikely that it constitutes a mere artefact produced by the opening of the gate.

Figure 5 presents the acquired flow fields for the three different initial depths $H_0 = 5$, 10 and 15 cm. The figures are scaled according to Froude similarity and are shown at the same non-dimensional time $t = 2$. Despite differences in the local flow structure, the observed phenomena exhibit a high degree of similarity in accordance with the analysis of §2.2. This can also be verified on figure 6, which plots the wave front trajectory in the non-dimensional (x, t)-plane for the three initial depths. The trajectory measurements fall on roughly the same curve for the three different initial depths. The outcome is (fortuitously) quite close to the experimental results obtained by Dressler (1954) for a dam-break wave of initial depth $H_0 = 11$ cm released over a very rough rigid bed (roughness elements composed of wooden sticks of square cross-section, 0.25 inch per side, placed transversely across the channel floor every inch). In the rigid bed case, the phenomena show a stronger dependence on the relative roughness (equivalent roughness over initial depth), as clearly exhibited in Dressler's results for different initial depths.

The theoretical assumptions can now be more precisely qualified. The highly uniform velocity profiles observed at the wave front validate our earlier statement that the average velocity of particles V_B at the wave tip can be taken equal to the vertically averaged velocity of the flow. In the upstream sheet-flow region, however, it is at best an approximation. The two-dimensional character of the flow is approximately

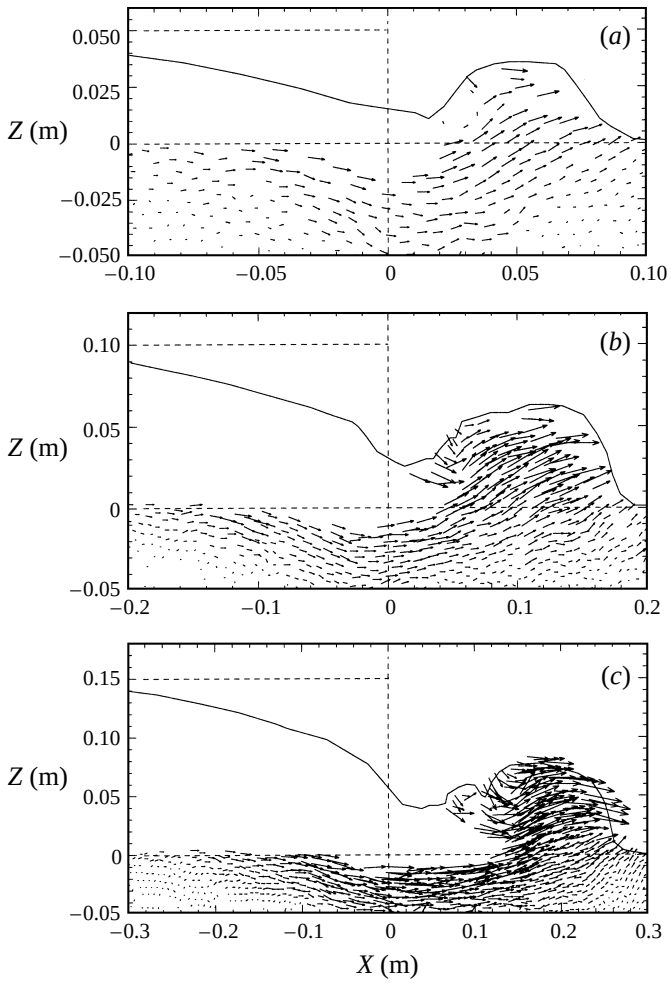

FIGURE 5. Free-surface profile and particle velocity field at dimensionless time $t = 2$: (*a*) initial depth $H_0 = 5$ cm; (*b*) $H_0 = 10$ cm; (*c*) $H_0 = 15$ cm; -----, initial gate position, bed profile and water surface.

verified. Limited non-uniformity of the transverse velocity profile due to sidewall effects was apparent at the wavefront, where centreline particles had velocities around 20% in excess of velocities observed near the wall. Most seriously, since the free-surface radius of curvature and scour hole length are in some regions of the same order as the flow depth, we expect the long-wave hypothesis to be applicable only in first approximation.

4. Comparison of numerical and experimental results

Solutions corresponding to the conditions of our experiments were obtained using the numerical scheme of §2.3. Adopting Bagnold's value of 0.32 for the dynamic friction factor $\tan\alpha$, two parameters are left to be calibrated. Non-dimensional sediment exchange and sediment mobility coefficients κ and ε were obtained by least squares fit from the measured sediment transport rates. Solutions are most sensitive to ε, while

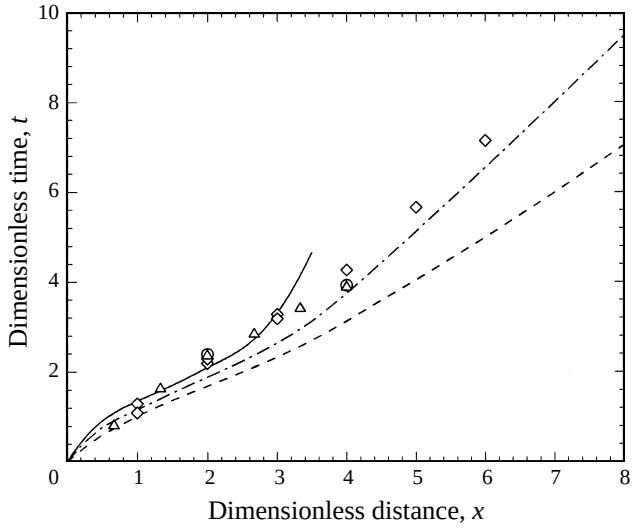

FIGURE 6. Experimental wavefront trajectories over rigid bed (Dressler 1954): ——, $H_0 = 5.5$ cm; —·—, $H_0 = 11$ cm; – – – –, $H_0 = 22$ cm; and over movable bed (present): ○, $H_0 = 5$ cm; ◇, $H_0 = 10$ cm; △, $H_0 = 15$ cm.

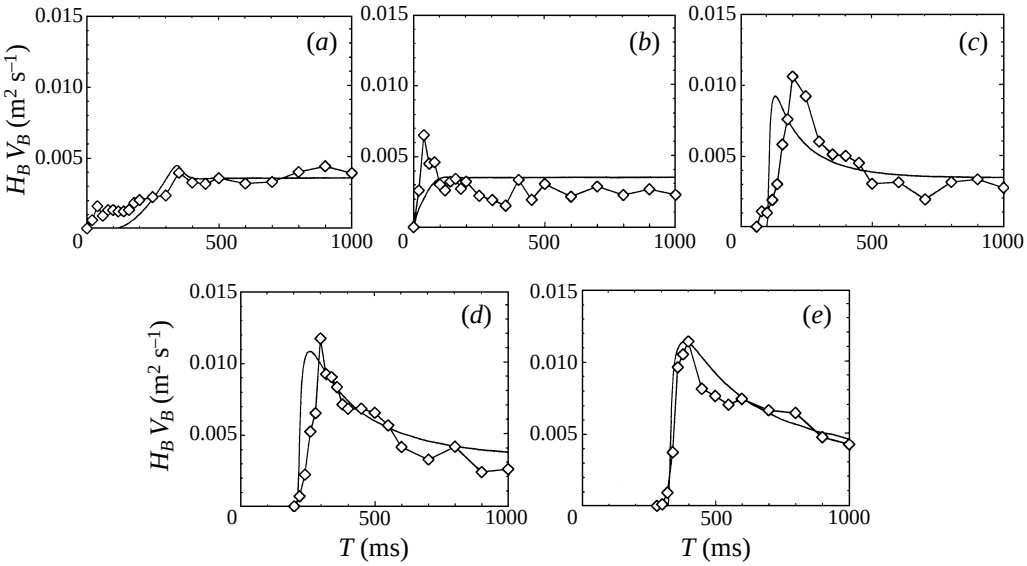

FIGURE 7. Sediment transport rates at various cross-sections for wave of initial depth $H_0 = 10$ cm: (*a*) $X = -10$ cm; (*b*) $X = 0$; (*c*) $X = 10$ cm; (*d*) $X = 20$ cm; (*e*) $X = 30$ cm; —◇—, measured; ——, computed.

κ exerts less influence on the results. The obtained calibrated values are

$$\kappa = 1.0, \quad \varepsilon = 0.4. \tag{4.1a,b}$$

For the computational results presented below, we adopted a spatial discretization of $\Delta X = H_0/25$ and a Courant number $Cr = 0.85$.

Experimental data and numerical solutions describing the sediment transport process can first be compared. Measured and computed results for the time evolution of the sediment transport rate are reported on figure 7. Data are given for selected

cross-sections along the flume and pertain to the dam-break wave of initial depth $H_0 = 10$ cm. The non-equilibrium sediment transport rates evaluated according to our simple relaxation relation agree reasonably well with the measurements. Maximum transport for each downstream cross-section is observed at the passage of the wavefront. However the front must travel a finite distance (≈ 20 cm) before seeing its sediment transport rate level off to its overall maximum value, and then decrease as frictional effects decelerate the wave. Ultimately, all sediment discharge hydrographs converge towards a common asymptote. This behaviour is described in a very similar way by the experimental and numerical results.

Various effects which are not included in the theoretical description can account for the slight discrepancies observed between the measured and computed sediment transport hydrographs. At cross-section $X = -10$ cm (figure 7*a*), pick-up of sediment occurs sooner than predicted by the computations. This is probably linked to the fact that the physical negative wave recedes upstream faster than the shallow-water description would indicate. This discrepancy is observed as well over a rigid bed, as shown by the profiles of figure 9. Also, a transient fluidization effect associated with the rapid drop in hydrostatic pressure experienced upstream at small times (Foda *et al.* 1997) could mobilize sediment before the shearing motion takes over as pick-up mechanism. At $X = 0$ (figure 7*b*), the measurements exhibit a salient peak which is not described by the computations. Examination of the images shows that this peak is simply due to the raising of the gate, with particles rushing in to fill the resulting void. At locations $X = 10$ and $X = 20$ cm, the peaks in sediment transport are underpredicted, as could be expected since vertical components of velocity are significant at those locations (see figure 4) and make sediment pick-up more severe. Finally, good agreement is obtained at section $X = 30$ cm, where the assumptions of the model are most closely met. In particular, as shown in figure 4(*c*), velocities are nearly horizontal in that region.

Sequences of free-surface and bed profiles are presented on figure 8. Measured profiles are given for the free surface, but not for the bed profiles since the distinct boundary between stationary bed and moving grains postulated by the theoretical approach corresponds in reality to a gradient region of varying particle packing and velocity through which drawing a line would be somewhat arbitrary. An approximate comparison can however be made by referring to figure 4. The overall profiles compare reasonably well with the experimental observations. Processes such as scour hole development, propagation of the steep wavefront and formation of the hydraulic jump are well described by the numerical solutions. As is common for computational results of shock-capturing schemes, the jump variation of the free surface is spread over a few grid points only. The physical jump, in contrast, extends over a length corresponding approximately to the flow depth.

In order to allow comparison between the sediment-bed case and the rigid-bed case, an equivalent sequence of surface profiles is shown in figure 9 for the dam-break wave over a smooth rigid bed. In that case, both theoretical and experimental profiles exhibit a purely monotonic decrease in height from the maximum in the undisturbed region to zero at the tip. On the whole, the contrasting features exhibited in figures 8 and 9 by dam-break waves over a movable granular bed and over a rigid bottom appear accurately predicted by the present model.

The detailed profiles, however, present significant deviations which we attribute mainly to limitations of the shallow-water description. At small times, vertical accelerations associated with the draw-down of the upstream water surface lead to discrepancies which are very similar in the sediment-bed and rigid-bed cases, whereby the edge of the negative wave recedes faster upstream than predicted by the shallow-

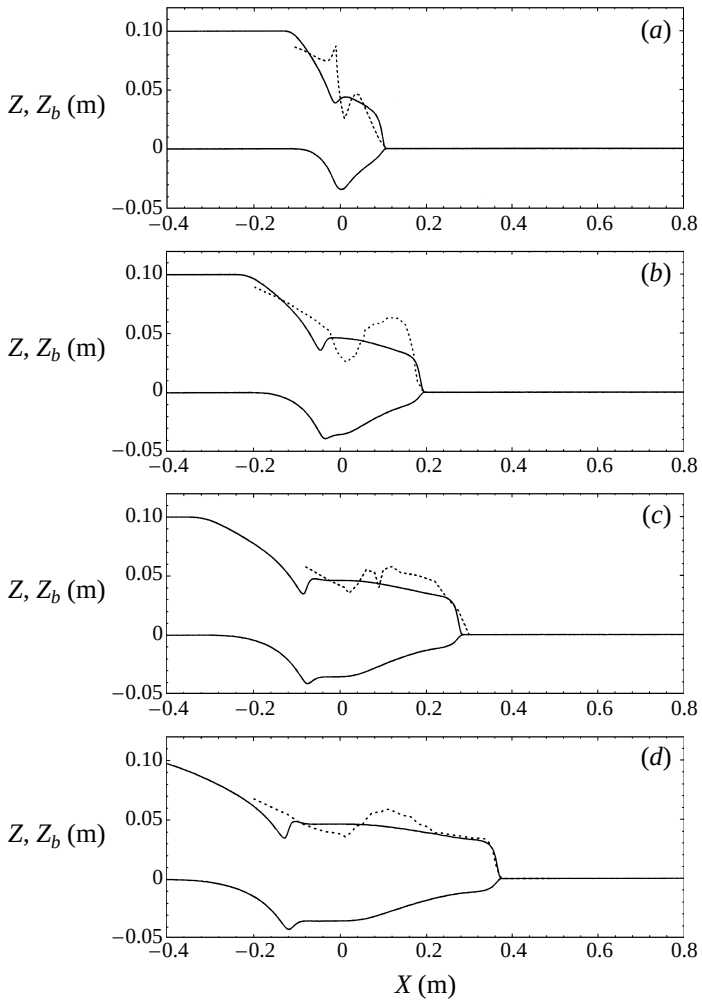

FIGURE 8. Surface profiles for the dam-break wave over movable granular bed (initial depth $H_0 = 10$ cm): (*a*) dimensionless time $t = 1$; (*b*) $t = 2$; (*c*) $t = 3$; (*d*) $t = 4$; - - - - -, measured free-surface profile; ——, computed free-surface and sediment bed profiles.

water theory. The sharp corner exhibited by the exact analytical solution is also rapidly smoothed out in the experimental profiles, presumably because of surface tension effects (Dressler 1954), and to a lesser extent in the computational solutions. From figure 9, it should be noted that the differences between theoretical and experimental results are much more important than the differences between computational and exact analytical solutions, indicating that the observed deviations arise mainly from approximations in the physical description, rather than from limitations of the numerical scheme. As analysed by Peregrine (1966), vertical accelerations cause the pressure field to depart from the assumed hydrostatic distribution. As a result, extra horizontal pressure gradients develop which lead to local deviations of the water profile from shallow-water solutions. The discrepancies observed in figures 8 and 9 appear consistent with this mechanism.

Over a granular bed, additional vertical accelerations are due, on the one hand, to the scour hole profile of the sediment bed, imprinting its curvature on the flow above,

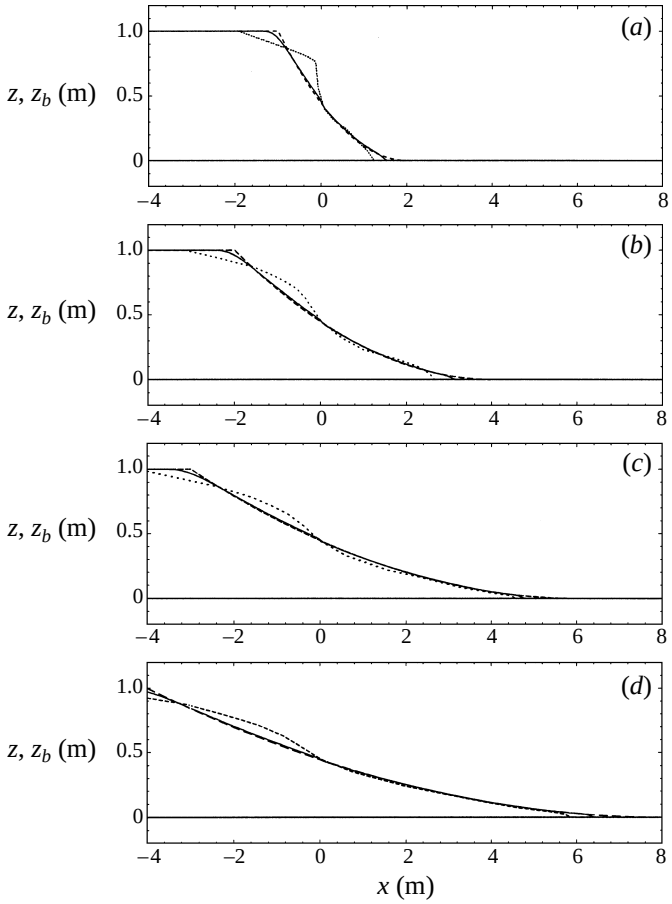

FIGURE 9. Surface profiles for the dam-break wave over smooth rigid bed: (*a*) dimensionless time $t = 1$; (*b*) $t = 2$; (*c*) $t = 3$; (*d*) $t = 4$; - - - - -, measured free-surface profile obtained by Dressler (1954) for a wave of initial depth $H_0 = 22$ cm over a smooth wood flooring; ——, computed free-surface profile and horizontal bed level; — — —, exact analytical solution for a wave over a frictionless bed (see Stoker 1957).

and on the other hand, to the rapidly varying surface associated with the hydraulic jump. This is probably the main reason why significant deviations are obtained for the amplitude and position of the hydraulic jump. As depicted in figure 8, the computed jump rapidly migrates upstream, whereas the observed one remains longer in the vicinity of the wave centre (at the original dam position). In contrast, better agreement is obtained for the front of the wave, both in trajectory and in profile. This is particularly the case at later times, when velocities are closer to horizontal at the wave tip (compare figures 8*d* and 4*c*). Further details concerning the jump and wavefront trajectories are provided below in §5, where an interpretation of the jump formation utilizing the theory of characteristics is also proposed.

5. Characteristics interpretation of the jump formation

Over a rigid horizontal bed, when resistance is neglected, the dam-break solution is a well known centred simple wave (Stoker 1948). A negative perturbation recedes upstream while a forward wavefront advances over the bed. Characteristic paths of

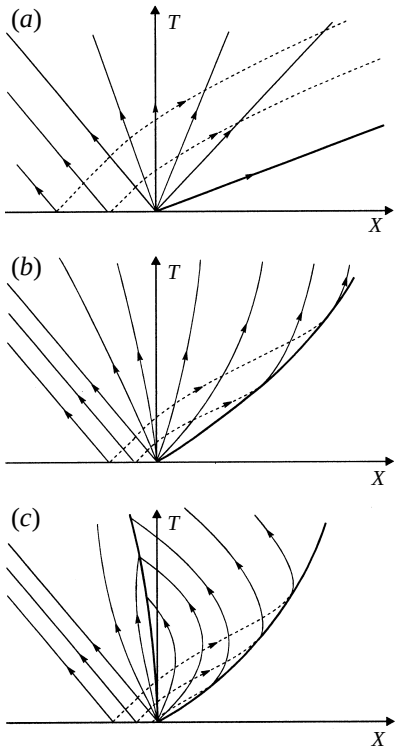

FIGURE 10. Pattern of hydrodynamic characteristics: (*a*) rigid, frictionless bed; (*b*) rigid bed with friction (after Dressler 1952); (*c*) mobile granular bed; - - - - -, along-current characteristics Λ_+; ——, counter-current characteristics Λ_-; ——, wavefront path and hydraulic jump trajectory.

the counter-current Λ_- family form a fan of straight rays having a common origin at the dam position (figure 10*a*). Resistance causes the Λ_- characteristic rays to bend in an upstream oriented curvature (Dressler 1952). The wavefront is then transformed from a double characteristic curve into an envelope of characteristics. Counter-current Λ_- characteristics branch out from the wavefront envelope as continuations of the along-current Λ_+ characteristics which join the envelope tangentially. This pattern is shown on figure 10(*b*).

For the dam-break wave over a granular bed, the edge of the negative wave recedes upstream exactly as over a rigid bed. The trajectory of the forward wavefront, however, is modified. The added inertia contributed by the eroded bed material and pore water combines with friction to decelerate the wavefront. For high-intensity transport, the inertial effects dominate and make the bending of characteristic rays very prominent at the wavefront.

Most notably, new effects arise due to bed deformation. Additional bending of the characteristics occurs due to gravity effects induced by the scour hole profile of the bed. The downstream adverse slope bends counter-current Λ_- characteristics even further upstream, while the upstream positive slope bends characteristics in the opposite direction, resulting in downstream oriented curvature. The net consequence is that characteristics of the Λ_- family now meet to form a secondary shock wave. A 'choking' of the flow therefore results near the wave centre. This conjecture for the mobile bed pattern of characteristics is shown on figure 10(*c*).

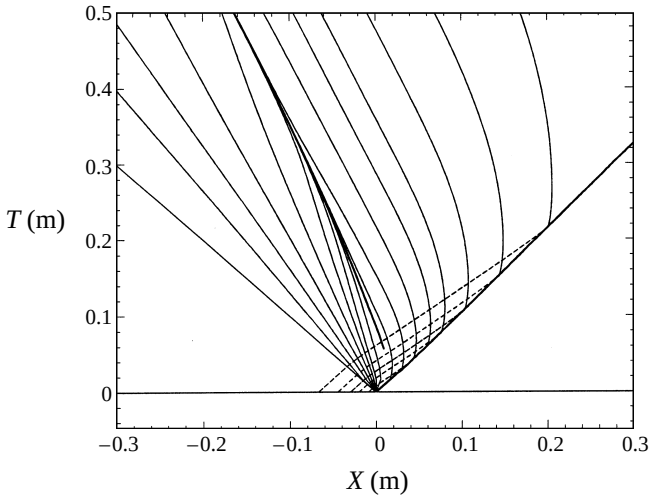

FIGURE 11. Paths of the hydrodynamic characteristics computed from numerical solutions: - - - - -, along-current characteristics Λ_+; ——, counter-current characteristics Λ_-; ——, wavefront path and hydraulic jump trajectory.

For verification, the numerical results were used to plot the hydrodynamic characteristic paths Λ_+ and Λ_- for the dam-break wave over a granular bed. This is shown on figure 11 to confirm the expected pattern. The hydrodynamic counter-current characteristics Λ_- are observed intersecting a shock path which coincides with the locus of the jump observed in the numerical free-surface profiles. The shock can now be understood more clearly as the result of significant bending of the Λ_- characteristics. The bending results from the effects of resistance and added inertia, as well as from slope effects due to scour hole development. The jump formation is thus shown to involve a strong interaction between the hydrodynamics of the dam-break wave and the morphodynamics of the granular bed.

Figure 12 shows the paths of the hydraulic jump and forward wavefront in the non-dimensional (x, t)-plane, in comparison with the experimental results. The jump location reference on the image sequences was fixed at the base of the jump, i.e. the local minimum in water surface level. In both the numerical and experimental results, the shock initially appears essentially stationary, remaining near the wave centre. This translates into a roughly vertical tangent at the origin of the (x, t)-plane. The jump then migrates upstream with accelerating celerity. Qualitatively, good agreement is found. Quantitatively, the trajectories correspond well for the wave of initial depth $H_0 = 5$ cm, but deviate somewhat for the other initial depths. Agreement is much better for the wavefront path, which fits closely the measurements regardless of initial depth H_0. Overall, the comparison lends confidence to our interpretation of the jump formation.

It is likely that the jump path constitutes one of the features that is most sensitive to limitations in the physical description of the flow. This appears to be the case more generally, beyond the present dam-break over a movable bed. In recent purely hydrodynamic benchmark tests performed for a dam-break wave propagating through a channel bend (CADAM 1998†), for instance, the most severe discrepancies and dispersion of results also arose in the description of a travelling hydraulic jump.

† Concerted Action on Dam-break Modelling (CADAM) is an EC funded Concerted Action Programme looking at dam-break modelling and application. Among other matters, the programme involves the comparison of numerical dam-break models and modelling procedures with analytical, experimental and field data.

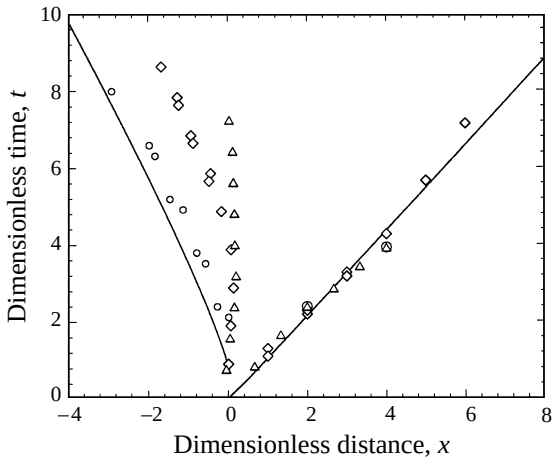

FIGURE 12. Forward wavefront and hydraulic jump paths in the (x, t)-plane: ○, measurements for wave of initial depth $H_0 = 5$ cm; ◇, $H_0 = 10$ cm; △, $H_0 = 15$ cm; ——, computations.

6. Summary and conclusions

The findings of the present study can be summarized as follows. First and foremost, the experimental and numerical results highlight a feature which strongly differentiates the dam-break wave over an erodible bed from its rigid bed equivalent. Over a granular bed, it was shown, the free surface breaks backward and a hydraulic jump forms near the wave centre.

The process involves a strong coupling between the hydrodynamics and morphodynamics of the flow–bed system, whereby the wave provokes an intense entrainment of material from the bed and the latter influences the flow in return through added inertia and gravity effects. The flow thus 'chokes' over a scour hole which it carves out beneath itself. From the standpoint of shallow-water theory, the jump formation can be interpreted as the result of bending and intersection of counter-current hydrodynamic characteristics.

Digital imaging was used to provide a detailed visualization of the system evolution, as well as obtain measurements for the free-surface profile, granular velocity field, and sediment transport rates. On the theoretical side, a vertically-averaged, non-equilibrium transport mathematical model was shown to successfully capture the main features of the flow. At the price of two calibration parameters pertaining exclusively to the transport process, reasonable quantitative agreement between measurements and numerical results was obtained. Rather encouraging is the fact that processes as diverse as non-equilibrium sheet and debris flow, scour hole development, wavefront propagation and jump formation could be described within a unified, relatively simple framework. Significant discrepancies were nonetheless recorded, and ascribed mainly to limitations of the shallow-water assumption.

As the transport intensity, depth of the scour hole, and strength of the shock vary primarily with the mobility of the bed material, the jump feature should not be as well defined over a natural sediment as over the light artificial particles used in the present experiments. Even low in magnitude, however, the jump is bound to challenge the limits of models. It is therefore important that frameworks adopted to handle fast shallow-water flows over mobile beds be robust enough to withstand the emergence of shocks.

Limitations of the theoretical description adopted in this study are twofold. First, no attempt was made to ground the empirical scalings on a detailed microscopic description of the intergranular contacts and fluid–grain interactions, such as could be provided by the recent advances of kinetic and microstructural theories (see the reviews of Campbell 1990, and Koenders 1997). Efforts to overcome this limitation should gain from the methods developed in the neighbouring field of non-equilibrium thermodynamics (see e.g. Dedeurwaerdere *et al.* 1996), possibly along the lines of the continuum thermodynamical approach applied to debris flow by Hutter, Svendsen & Rickenmann (1996).

A second restriction is due to the long-wave approximation underlying the theoretical approach. The adopted shallow-water description accounts for neither the effects of vertical accelerations nor those linked to the vertical structure of the flow (i.e. the distributions of velocities, granular concentrations and stresses over a vertical). Without resorting to a truly multidimensional description, the extension of shallow-water theory to moderately shallow flows (see Steffler & Jin 1993) could prove a useful strategy to make progress in this respect.

Finally, such endeavours should benefit much from a close interaction with experimental research, exploiting in particular the current developments in measurement techniques. These various points are considered for future work.

The authors gratefully acknowledge the contribution of H. H. Liu and X. Van Crombrugghe to the experimental work described herein. Financial support for the instrumentation was provided by the National Science Council of the Republic of China under grant no. 85-2611-E-002-005. Most of the present research was carried out while the first writer was a graduate student at the National Taiwan University supported by a scholarship from the Ministry of Education of the Republic of China. The authors wish to thank X. Sillen, Professor Y. Zech and Professor P. Habets of the Université Catholique de Louvain, Belgium, for helpful discussions. We are also grateful to the anonymous referees for their suggestions and challenging comments. Finally, we are deeply indebted to Professor D. H. Peregrine for pointing out a major problem in our original interpretation of the jump feature.

REFERENCES

Abbott, M. B. 1979 *Computational Hydraulics, Elements of the Theory of Free Surface Flows*. Pitman.

Adriaens, F. & Rillaer, L. van 1996 The feasibility of two-dimensional particle tracking velocimetry for the study of vertical sediment transport in a turbulent free surface flow. B. Eng. Thesis, Technische Universiteit Delft, The Netherlands.

Adrian, R. J. 1991 Particle-imaging techniques for experimental fluid mechanics. *Ann. Rev. Fluid Mech.* **23**, 261–304.

Asano, T. 1995 Sediment transport under sheet-flow conditions. *J. Waterway Port Coast. Ocean Engng* **121**, 239–246.

Bagnold, R. A. 1954 Experiments on a gravity-free dispersion of large solid spheres in a Newtonian fluid under shear. *Proc. R. Soc. Lond.* A **225**, 49–63.

Bagnold, R. A. 1956 The flow of cohesionless grains in fluids. *Phil. Trans. R. Soc. Lond.* A **249**, 235–297.

Bauer, E. G., Houdayer, G. R. & Sureau, H. M. 1976 A non-equilibrium axial flow model in application to loss-of-coolant accident analysis. *OECD/NEA Specialist Meeting on Transient Two-phase Flow, Toronto, Canada.*

Benjamin, T. B. & Lighthill, M. J. 1954 On cnoidal waves and bores. *Proc. R. Soc. Lond.* A **224**, 448–460.

Braschi, G. & Gallati, M. 1992 A conservative flux prediction algorithm for the explicit computation of transcritical flow in natural streams. In *Hydraulic Engineering Software IV: Fluid Flow Modelling* (ed. W. R. Blain & E. Cabrera), pp. 381–394. Computational Mechanics Publications & Elsevier.

Concerted Action on Dam-break Modelling (CADAM) 1998 *First Meeting of the European Concerted Action on Dam-break Modelling*, Wallingford, *UK, March 1998*. Proceedings to be published.

Campbell, C. S. 1990 Rapid granular flows. *Ann. Rev. Fluid Mech.* **22**, 57–92.

Capart, H. 1996 Non-equilibrium sediment transport under shallow-water waves. MSc Thesis, National Taiwan University, Taipei, Taiwan.

Capart, H., Liu, H. H., Van Crombrugghe, X. & Young, D. L. 1997 Digital imaging characterization of the kinematics of water-sediment interaction. *Water Air Soil Pollut.* **99**, 173–177.

Capart, H., Sillen, X. & Zech, Y. 1997 Numerical and experimental water transients in sewer pipes. *J. Hydr. Res.* **35**, 659–672.

Capart, H. & Young, D. L. 1997 Validation of digital imaging measurements of high-intensity sediment transport. In *Proc. Ninth Intl Conf. on Transport and Sedimentation of Solid Particles* (ed. J. Sobota), pp. 265–276. Publ. Univ. of Agriculture, Wrocław, Poland.

Dedeurwaerdere, T., Casas-Vazquez, J., Jou, D. & Lebon, G. 1996 Foundations and applications of a mesoscopic thermodynamic theory of fast phenomena. *Phys. Rev.* E **53**, 498–506.

Dick, J. E. & Sleath, J. F. A. 1991 Velocities and concentrations in oscillatory flow over beds of sediment. *J. Fluid Mech.* **233**, 165–196.

Dressler, R. F. 1952 Hydraulic resistance effect upon the dam-break functions. *Nat. Bur. Stand. J. Res.* **49**, 217–225.

Dressler, R. F. 1954 Comparison of theories and experiments for the hydraulic dambreak wave. In *Assemblée Générale de Rome*, vol. 3, pp. 319–328. Intl Assoc. of Hydrology.

Einstein, A. 1920 Uber Schallschwingungen in teilweise dissoziierten Gasen. *Sitzung Berl. Akad. Physik Chemie* **380**.

Einstein, H. A. 1950 The bed-load function for sediment transportation in open-channels. *US Dept. of Agriculture Tech. Bull.* 1026.

Fernandez-Luque, R. & Beek, R. van 1976 Erosion and transport of bedload sediment *J. Hydr. Res.* **14**, 127–144.

Foda, M. A., Hill, D. F., DeNeale, P. L. & Huang, C. M. 1997 Fluidization response of sediment bed to rapidly falling water surface. *J. Waterway Port Coast. Ocean Engng* **123**, 261–265.

Fredsøe, J. & Deigaard, R. 1992 *Mechanics of Coastal Sediment Transport*. World Scientific.

Harten, A., Lax, P. & Leer, A. van 1983 On upstream differencing and Godunov-type schemes for hyperbolic conservation laws. *SIAM Rev.* **25**, 35–61.

Havnø, K. 1995 Danish Hydraulic Institute research and consultancy in the field of river sediment transport. Seminar presentation, Taipei, October 3, 1995.

Hirano, M. & Iwamoto, M. 1981 Experimental study on the front of debris flow. *Shin-Sabo* **121**, 1–7 (in Japanese).

Hutter, K., Svendsen, B. & Rickenmann, D. 1996 Debris flow modeling: A review. *Continuum Mech. Thermodyn.* **8**, 1–35.

Jähne, B. 1991 *Digital Image Processing*. Springer.

Jain, R., Kasturi, R. & Schunck, B. G. 1995 *Machine Vision*. McGraw-Hill.

Kevorkian, J. 1990 *Partial Differential Equations: Analytical Solutions Techniques*. Wadsworth & Brooks/Cole.

Koenders, M. A. 1997 A first order constitutive model for a particulate suspension of spherical particles. *Acta Mech.* **122**, 1–19.

Lax, P. D. 1954 Weak solutions of nonlinear hyperbolic equations and their numerical computation. *Commun. Pure Appl. Maths* **7**, 159–193.

Lee, H. Y. & Hsu, I. S. 1994 Investigation of saltating particle motions. *J. Hydr. Engng* **120**, 831–845.

Liggett, J. A. 1994 *Fluid Mechanics*. McGraw-Hill.

Lin, J. C. & Rockwell, D. 1995 Evolution of a quasi-steady breaking wave. *J. Fluid Mech.* **302**, 29–44.

Longuet-Higgins, M. S. 1992 Capillary rollers and bores. *J. Fluid Mech.* **240**, 659–679.

Nakagawa, H., Tsujimoto, T. & Gotoh, H. 1992 Stochastic simulation of bed-load transport under

oscillation-current coexisting flow. In *Proc. Sixth Intl Symp. on Stochastic Hydraulics* (ed. J. T. Kuo & G. F. Lin), pp. 197–204. Dept of Civil Engng, National Taiwan University.

Nakagawa, H., Tsujimoto, T. & Miyamoto, H. 1978 16mm film analysis of characteristic quantities of bed load transport. *Kyoto University, Disaster Prevention Research Institute, Annuals* **20b**, 355–370 (in Japanese).

Nnadi, F. N. & Wilson, K. C. 1992 Motion of contact-load particles at high shear stress. *J. Hydr. Engng* **118**, 1670–1684.

Peregrine, D. H. 1966 Calculations of the development of an undular bore. *J. Fluid Mech.* **25**, 321–330.

Phillips, B. C. & Sutherland, A. J. 1989 Spatial lag effects in bed load sediment transport. *J. Hydr. Res.* **27**, 115–133.

Reif, F. 1965 *Fundamentals of Statistical and Thermal Physics*. McGraw-Hill.

Ribberink, J. S. & Al-Salem, A. 1990 Bedforms, sediment concentration and sediment transport in simulated wave conditions. In *Proc. 22nd Intl Coastal Engng Conf.* (ed. B. L. Edge), pp. 2318–2331. ASCE.

Steffler, P. M. & Jin, Y. 1993 Depth averaged and moment equations for moderately shallow free surface flow. *J. Hydr. Res.* **31**, 5–17.

Stoker, J. J. 1948 Formation of breakers and bores. *Commun. Pure Appl. Maths* **1**, 1–87.

Stoker, J. J. 1957 *Water Waves*. Interscience.

Sumer, B. M., Kozakiewicz, A., Fredsøe, J. & Deigaard, R. 1996 Velocity and concentration profiles in sheet-flow layer of movable bed. *J. Hydr. Engng* **122**, 549–558.

Suwa, H. 1988 Focusing mechanisms of large boulders to a debris-flow front. *Trans. Japanese Geomorphological Union* **9**, 151–178.

Takahashi, T. 1991 *Debris flow*. IAHR & Balkema.

Takahashi, T. & Nakagawa, H. 1994 Flood/debris flow hydrograph due to collapse of a natural dam by overtopping. *J. Hydrosc. Hydr. Engng* **12**, 41–49.

Tsubaki, T. & Saito, T. 1967 Regime criteria for sand waves in erodible bed channels. *Kyushu University, Faculty of Engineering, Annuals* **40**, 741–748 (in Japanese).

US Department of the Interior, Bureau of Reclamation 1996 Glen Canyon Dam beach/habitat-building test flow. Draft Environmental Assessment and Draft Finding of No Significant Impact.

Visser, P. J., Vrijling, J. K. & Verhagen, H. J. 1990 A field experiment on breach growth in sand-dikes. In *Proc. 22nd Intl Coastal Engng Conf.* (ed. B. L. Edge), pp. 2087–2100. ASCE.

Waythomas, C. F., Walder, J. S., McGimsey, R. G. & Neal, C. A. 1996 A catastrophic flood caused by drainage of a caldera lake at Aniakchak Volcano, Alaska, and implications for volcanic hazards assessment. *Geol. Soc. Am. Bull.* **108**, 861–871.

Whitham, G. B. 1974 *Linear and Nonlinear Waves*. Wiley.

Wilson, K. C. 1987 Analysis of bed-load motion at high shear stress. *J. Hydr. Engng* **113**, 97–103.

Yalin, M. S. 1972 *Mechanics of Sediment Transport*. Pergamon.